SMALL DISTURBANCE NAVIER-STOKES COMPUTATIONS FOR LOW ASPECT RATIO WING PITCHING OSCILLATIONS

Alexander Pechloff * , **Boris Laschka** †
Technische Universität München, Boltzmannstr. 15, D-85748 Garching, Germany

Keywords: *small disturbance Navier-Stokes equations, computational fluid dynamics, aeroelasticity*

Abstract

For dynamic production aeroelastic analysis in the transonic speed range a computational fluid dynamics (CFD) method based on the small disturbance Navier-Stokes equations can serve as a reasonable alternative to one realizing the Reynolds-averaged Navier-Stokes (RANS) equations' time domain solution: Its dynamically linear approach promises significantly decreased computation cost in the prediction of unsteady aerodynamic loading while retaining the latter's fidelity to a high degree. In this regard, research conducted at the Technische Universität München has resulted in the CFD method FLM-SD.NS. Further substantiating its application readiness, computations for harmonic pitching oscillations of the NASA clipped delta wing are presented. Test cases are characterized by shocks of varying strength and range of motion, as well as leading edge vortex (LEV) formation. Overall, results are in good agreement with dynamically fully nonlinear solutions provided by the comparative RANS solver FLM-NS, as well as available experimental data. Reductions in computation time up to an order of magnitude in relation to FLM-NS are observed. Limitations of the small disturbance approach, however, become apparent for the LEV case, where higher-order harmonics are far less negligible in the flow's response to the excitation.

Nomenclature

A	=	semi-span planform area, $\int_0^s c\,dy$
c	=	local chord length, $c(y/s)$
c_L	=	lift coefficient, dimensional lift normalized with $\check{\rho}_\infty \lvert\check{\mathbf{v}}_\infty\rvert^2 \check{A}/2$
c_M	=	moment coefficient, dimensional moment respective the pitch axis normalized with $\check{\rho}_\infty \lvert\check{\mathbf{v}}_\infty\rvert^2 \check{A}\check{c}_\mu/2$ (>0: tail-heavy moment)
c_{av}	=	average chord length, A/s
c_p	=	pressure coefficient
$c_{p,crit}$	=	critical pressure coefficient, $c_p(Ma_\infty)$ at $Ma = 1.0$
c_r	=	root chord length, $c(0)$
c_t	=	tip chord length, $c(1)$
c_μ	=	reference chord length, $\int_0^s c^2\,dy/A$
d^+	=	sublayer-scaled distance of the first off-body grid plane
f	=	oscillation frequency
Im	=	imaginary part, normalized with $\check{\alpha}\pi/180$ deg
k_{red}	=	reduced oscillation frequency, $2\pi\check{f}\check{L}\sqrt{\check{\rho}_\infty}/(Ma_\infty\sqrt{\gamma\check{p}_\infty})$
L	=	reference length of the geometric nondimensionalization
Ma	=	local Mach number
Ma_∞	=	freestream Mach number, $\lvert\check{\mathbf{v}}_\infty\rvert\sqrt{\check{\rho}_\infty}/\sqrt{\gamma\check{p}_\infty}$
Pr	=	Prandtl number
Pr_t	=	turbulent Prandtl number
p_∞	=	freestream static pressure
Re	=	real part, normalized with $\check{\alpha}\pi/180$ deg
Re_∞	=	freestream Reynolds number,

* Dipl.-Ing. Univ., Research Engineer
† Prof. em. Dr.-Ing.

		$\check{\rho}_\infty \lvert\check{\mathbf{v}}_\infty\rvert \check{c}_{av}/\check{\mu}_\infty$
s	=	semi-span length
T_∞	=	freestream static temperature
t	=	time
t_{CPU}^{method}	=	FLM method's computation time
$\lvert\mathbf{v}_\infty\rvert$	=	magnitude of the freestream velocity vector
x, y, z	=	global Cartesian coordinates
x	=	span-station-local chordwise coordinate, $x(y/s)$ (= 0: leading edge, = c: trailing edge)
x_d	=	x of a wing section's maximum thickness
x_p, z_p	=	global pitch axis coordinates
y	=	semi-span coordinate (= 0: root, = s: tip)
α	=	incidence angle
γ	=	ratio of specific heats
Δ	=	difference between lower- and upper-surface value
λ	=	taper ratio, c_t/c_r
μ	=	molecular viscosity, governed by Sutherland's law
μ_∞	=	freestream molecular viscosity, $\mu(T_\infty)$
ρ_∞	=	freestream density
τ_s	=	characteristic time, $\check{t}\,Ma_\infty\sqrt{\gamma\check{p}_\infty}/(\check{L}\sqrt{\check{\rho}_\infty})$
ζ_{CPU}	=	ratio of computation times, $\check{t}_{CPU}^{SD.NS}/\check{t}_{CPU}^{NS}$
$\mathcal{AR}$	=	semi-span aspect ratio, s^2/A

Superscripts

0	=	zeroth harmonic
1	=	first harmonic
2, 3	=	second, third harmonic
$\bar{}$	=	time-invariant mean
$\hat{}$	=	perturbation amplitude
$\check{}$	=	dimensional

1 Introduction

To date production analysis of an aircraft's dynamic aeroelastic behavior relies on low-order computational fluid dynamics (CFD) methods to supply the unsteady aerodynamic structural loading. This approach has proven to be highly efficient and of excellent fidelity in the sub- and supersonic speed range. In the transonic speed range, however, which is the flight envelope's most critical respective stability, these methods fail to produce adequate predictions as convective nonlinearities and viscous effects generally remain unaccounted for. A CFD method realizing the Reynolds-averaged Navier-Stokes (RANS) equations' time domain solution, on the other hand, would be well suited to render the unsteady aerodynamic loading most accurately, as such flow properties are naturally inherent to the formulation. Unfortunately, this type of high-order CFD method becomes computationally prohibitive when confronted with the multitude of parameter variations (Ma_∞, Re_∞, $\check{\alpha}$, $\check{\bar{\alpha}}$, k_{red}, eigenmode) required by the analysis [10].

Dual time-stepping schemes typically employed in the RANS equations' time domain solution must sequentially realize a pseudo-steady solution at each incremental deflection of the considered body's oscillatory motion. In this manner the flow's response to an imposed excitation is rendered as a series of time-accurate snap-shots. For an individual cycle the number of pseudo-steady solutions equals the number of physical time-intervals utilized in its discretization, as dictated by a sufficient temporal resolution of the unsteady flowfield. Obtaining the desired periodicity, however, always involves the computation of a number of cycles, a circumstance which becomes especially time-consuming at low frequencies. The aggregate number of pseudo-steady solutions then represents the primary cost of the dual time-stepping approach.

A secondary one rests in the accompanied incremental deformation of the body-embedding computational grid. For each physical time-step the computational grid must be updated to the body's new position, a task which contributes all the more to the total computational cost as the geometric complexity of the body increases. Lastly, the effort associated with the acquired data's post processing has to be taken into account. Since the unsteady loading is gained as a series in time, subsequent Fourier analysis becomes necessary

to extract the harmonics of interest. In doing so, turnaround time and thus throughput of the overall process is further diminished. Whereas the computational cost of this approach may be tolerable for an individual case, it becomes too high in the cumulation of production investigations.

Promising significantly decreased cost while yet retaining the fidelity of the RANS equations' time domain solution to a high degree, a CFD method based on the small disturbance Navier-Stokes equations can serve as a reasonable alternative: For problems of dynamic stability the considered body's neutral motion can be regarded as being limited to minor harmonic deflections about a reference position. Consequently, the organized unsteadiness inherent to the flowfield's instantaneous response can be presumed to be a predominantly dynamically linear perturbation about a time-invariant mean state. This would entail that higher-order harmonics present within the response become negligible to the point where a generally phase-shifted first harmonic prevails. Under the preceding assumption, a system of statistically treated linear partial differential equations exclusively governing the organized unsteadiness can be extracted from the instantaneous Navier-Stokes equations. Insertion of a simple harmonic time law then allows the novel equation system to be brought into a frequency domain formulation, eliminating time-dependency altogether. Thus, time-accuracy and the accompanied incremental grid deformation are no longer an issue to the solution process, the necessary computational effort becoming comparable to the one involved with the steady-state solution of the RANS equations.

Rendered in terms of complex amplitude field variables, the frequency domain solution embodies magnitude and phase-shift of the organized unsteadiness. It develops contingent on the a priori known oscillation frequency and amplitude deflection of the considered body's harmonic motion, as well as the reference (time-invariant mean) flowfield about which the organized unsteadiness is consider to occur. The frequency and amplitude deflection may yield from structural modal analysis, with the latter numerically supplied to the method by way of two computational grids, respectively, embedding the body at its reference and deflected extremum position. A steady-state RANS solution realized in the reference grid for the defined freestream conditions then serves as the time-invariant mean flowfield. Dynamically nonlinear phenomena that would emerge in the flowfield's instantaneous response are approximately handled as dynamically linear perturbations about a statically nonlinear state, as contained in the time-invariant flowfield. Contrary to the time domain (dynamically fully nonlinear) approach, the first harmonic of the unsteady loading is gained directly, being considered equal to the obtained complex amplitude load under the small disturbance premise. Similarly, the zeroth harmonic is seen as equal to the afore computed time-invariant mean loading.

Over the past decade, research conducted at the former Aerodynamics Division of the Institute for Fluid Mechanics (FLM)[‡], Technische Universität München, has ultimately resulted in the small disturbance Navier-Stokes method FLM-SD.NS. Its two-dimensional incarnation for high-Reynolds-number flow was originally presented in [8], where a detailed derivation of the underlying governing equations, as well as a synopsis of the general properties and computation process is given. Airfoil test cases demonstrated the approach's validity in the transonic regime. The introduction of the third spatial coordinate is straightforward and has been completed since then. FLM-SD.NS itself had been realized as the viscous extension of the already well established small disturbance Euler method FLM-SDEu [6]. An effort had been made to retain numerical equivalence to the in-house RANS method FLM-NS [1], which is utilized, on the one hand, to supply the necessary time-invariant mean flowfield to FLM-SD.NS, while on the other hand, to render a dynamically fully nonlinear solution of the particular unsteady case for comparative purposes. Consequently, the cell-centered structured finite volume method FLM-SD.NS (multiblock capable) features small

[‡]reconstituted as the Institute of Aerodynamics in 12/04

disturbance instances of Roe's convective flux-difference splitting [9] and of Chakravarthy's viscous flux evaluation [4]. Second-order spatial accuracy is given for smoothly stretched grids and regions of continuous flow, with the total variation diminishing condition yet satisfied at locations of discontinuity. A compliant derivation of the Spalart-Allmaras (S/A) turbulence model provides eddy viscosity closure, while a multigrid embedded lower-upper symmetric successive overrelaxation (LU-SSOR) scheme adapted from Blazek [3] integrates the discretized governing equations in pseudo-time.

Initial three-dimensional FLM-SD.NS computations were conducted for harmonic flap oscillations of both the NASA clipped delta wing (NCDW) [2] and a fighter type delta wing (FTDW) in actual service [11] under high-Reynolds-number transonic flow conditions. Select results thereof were presented in [5], establishing the method's accuracy and efficiency. Reductions in computation time up to an order of magnitude in relation to FLM-NS were ascertained. Further substantiating the application readiness of FLM-SD.NS, computations for NCDW harmonic pitching oscillations under equivalent flow conditions are realized. The imposed motion is governed by

$$\breve{\alpha}(\tau_s) \;=\; \breve{\bar{\alpha}} \;+\; \breve{\hat{\alpha}} \cdot \sin(k_{red} \cdot \tau_s) \qquad (1)$$

about the given pitch axis, with $\breve{\bar{\alpha}}$, $\breve{\hat{\alpha}}$, and k_{red} set through the individual test case. The local unsteady load distribution normal to the wing's surface, embodied by c_p^0, c_p^1, as well as the resultant global loading, expressed by c_L^0, c_L^1 and c_M^0, c_M^1, are investigated. The latter directly result from the integration of the c_p^0, c_p^1 and correspondent skin-friction distributions over the wing's reference position surface. Prediction quality of FLM-SD.NS is primarily assessed by comparing its directly gained results to those yielding from Fourier-analyzed FLM-NS time series: The discrete evolution of c_L and c_M result from the integration of the c_p and skin-friction distributions over the deflected wing's surface after each converged physical time step. Additionally, inviscid results computed with FLM-SDEu and the underlying dynamically fully nonlinear Euler method FLM-Eu [6] are drawn upon to emphasize the impact of viscosity. Both FLM-NS and FLM-Eu render the unsteady aerodynamic loading with second-order accuracy in time. Experimental surface pressure data are also taken into account.

The globally utilized Cartesian coordinate system is set to originate (at reference position) from the wing's root leading edge (LE), with the x (chordwise) direction running positively towards the trailing edge (TE) and the y (spanwise) direction running positively towards the starboard tip. The imposed motion is strictly longitudinal, that is, occurring about an axis parallel to the spanwise direction. Consequently, a semi-span numerical treatment of the NCDW suffices, the starboard half being considered here.

2 NASA Clipped Delta Wing

Derived from the wing of a tentative supersonic transport, the NCDW is characterized by a 50.4 deg swept LE, an unswept TE, and a symmetrical circular arc section of constant 6 % relative thickness across the span ($x_d/c = 0.5$, sharp LE / TE), sans twist. In its semi-span instance ($\breve{L} := \breve{s} = 1.145$ m) the planform is trapezoidal, with $s := \breve{s}/\breve{L} = 1.0$ and $c_r := \breve{c}_r/\breve{L} = 1.410$ supplementing the sweep angles in the definition. The secondary geometric properties result to $\lambda = 0.142, A = 0.805, \mathcal{AR} = 1.242, c_{av} = 0.805$, and $c_\mu = 0.956$, while the pitch axis resides at $x_p/c_r = 0.65$ and $z_p = 0.00$. Surface pressure distributions are evaluated at six distinct span stations, of which all but the innermost correspond to those instrumented on the test model. Data for merely one inner and one outer span station, $y_{s2} := y/s = 0.33$ and $y_{s5} = 0.69$, respectively, will be discussed.

The upper and lower surface of the NCDW's numerical embodiment are each discretized with 72 cells (hyperbolically distributed) in chordwise and 32 cells (Poisson-distributed) in spanwise direction for a total of 2304 cells per surface (Fig. 1). It is embedded (at reference position) in an elliptically smoothed two block C-H-topology

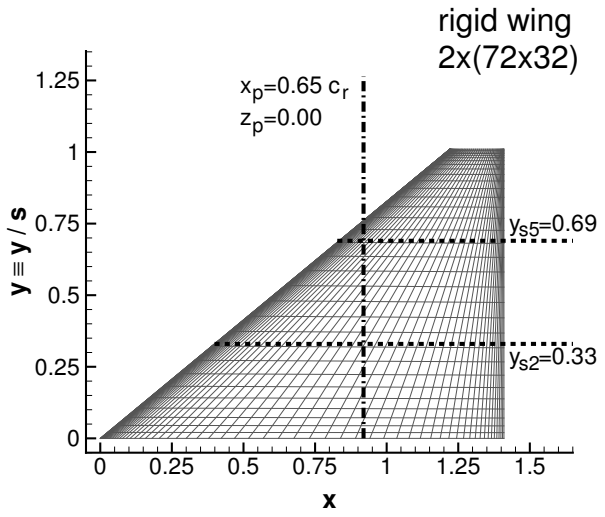

Fig. 1 NCDW semi-span surface grid with superimposed pitch axis and investigated span stations

structured volume grid by way of a curvilinear boundary-fitted coordinate system. The far-field distances are set to $11 \times s$ in positive chordwise direction from the root LE, to $11 \times s$ in both positive and negative vertical (z) direction from the root TE, as well as to $5 \times s$ in spanwise direction respective the wing's lateral (xz) plane of symmetry. Each block discretizes one half of the numerically treated physical domain as divided by the wing's vertical (xy) plane of symmetry. Thus, the individual block is associated with strictly one of the wing's surfaces, either the upper or lower. It discretizes the delimited volume with 96 cells in positive chordwise, 48 cells in spanwise, and 40 cells in wing surface normal direction, translating into 184320 cells per block or 368640 cells for the entire grid. Cells in wing surface normal direction are hyperbolically distributed, the distance of the first off-body grid plane being set to $1 \times 10^{-5} \times s$. For the considered high-Reynolds-number transonic flow this renders $d^+ < 5$ as required by the Spalart-Allmaras turbulence model. The chosen two block topology allows orthogonality of grid lines emanating from the upper and lower surface in proximity to the leading edge. Regeneration of the volume grid for the amplitude-deflected surface grid and subsequent smoothing ultimately yields the desired extremum grid. Hence, its global properties are equivalent to those of the reference grid. Further details on grid construction and smoothing are given in [7].

From the multitude of computed dynamic test cases, results for a weak shock case (90D5), the medium strength shock / leading edge vortex (LEV) case (90D29), and a strong shock case (94D5) are presented. Table 1 provides the computation parameters, while Tab. 2 specifies the values of the dimensional thermodynamic reference quantities complementing $\check{L}$. All cases have $Re_\infty \approx 10.0 \times 10^6$, $\gamma = 1.132$, $Pr = 0.775$ (heavy gas), and $Pr_t = 0.90$ in common. Test case 90D5 will serve as baseline.

Case	Ma_∞	$\check{\alpha}$, deg	$\check{\alpha}$, deg	k_{red}	$\check{f}$, Hz
90D5	0.90	0.00	0.50	0.237	8.0
90D29	0.90	3.97	0.50	0.240	8.0
94D5	0.94	0.00	0.50	0.230	8.0

Table 1 Computation parameters of the NCDW cases

Case	$\check{p}_\infty$, kPa	$\check{\rho}_\infty$, kg/m^3	$\check{T}_\infty$, K
90D5	20.7	0.326	298.4
90D29	20.5	0.329	298.9
94D5	19.3	0.313	295.5

Table 2 Values of the NCDW cases' dimensional thermodynamic reference quantities

FLM-SD.NS computations employ a three-level V-symmetric multigrid cycle for acceleration. Per multigrid cycle dual pseudo-time steps on the finest and coarsest grid level in combination with a single pseudo-time step on the intermediary level (2/1/2) are conducted. A converged solution of the governing equations is ascertained if the L_2-norm amplitude density residual, as normalized with its value after the first multigrid cycle, has dropped below 5.5×10^{-4} (5.0×10^{-4} for 90D29), terminating the computation. Instability of the solution process was

initially experienced for 94D5, where a confined region of post-shock separation occurs towards the wing tip in the supplied time-invariant mean flowfield. The localized limitation of the amplitude S/A working variable, however, allowed for a simple remedy. Comparative FLM-NS computations consider three oscillation cycles to eliminate transient phenomena, each discretized with 100 physical time intervals. Incremental grid deformation is carried out through time-law-accordant interpolation between the extremum and reference grid. Multigrid parameters and abort criterion are set equal to those of the FLM-SD.NS computations. In postprocessing, Fourier analysis of the c_p-, c_L-, and c_M-time-series, ascertained to be periodic for the third cycle, yields the respectively inherent zeroth and first harmonic. FLM-SD.NS / FLM-NS computation of 90D5, and 90D29, were conducted on a single 1.3 GHz Intel®Itanium®2 processor of the Leibniz Rechenzentrum (LRZ) Linux cluster, with 94D5 subsequently realized on a 1.6 GHz successor model.

Generally, the supplemental FLM-SDEu / FLM-Eu computations employ the same reference and extremum grid as the FLM-SD.NS / FLM-NS ones in order to retain spatial comparability. For 90D29, however, the high resolution of the wing-near field destabilized the inviscid solution process, necessitating the consideration of more Euler-typical grids. These are internally generated from the Navier-Stokes grids through elimination of every other cell edge, rendering coarser grids of merely 46080 cells. Nevertheless, the wing surface and near-field remains sufficiently resolved, as the distance of the first off-body grid plane only increases to $3 \times 10^{-5} \times s$ and the first five of 20 cells in wing surface normal direction reside within $1 \times 10^{-3} \times s$.

It should be noted, that the experimental surface pressure data of the dynamic test cases are limited to the first harmonic. Thus, for zeroth harmonic comparison the experimental surface pressure data of the underlying static test case are drawn upon. Each represents the NCDW investigated under congruous ambient conditions yet fixed at its time-invariant mean incidence angle. For 90D5, 90D29, and 94D5, these are 90S1, 90S38, and 94S1, respectively.

3 Results and Discussion

3.1 Weak Shock Case

For $Ma_\infty = 0.90$, $Re_\infty = 10.13 \times 10^6$, and $\breve{\alpha} = 0.0$ deg the FLM-NS supplied time-invariant mean flowfield exhibits a localized, equally developed supersonic region in proximity to the upper and lower wing surface. It extends, respectively, from the root to the tip, terminating with a weak shock significantly upstream of the TE (Fig. 2). FLM-

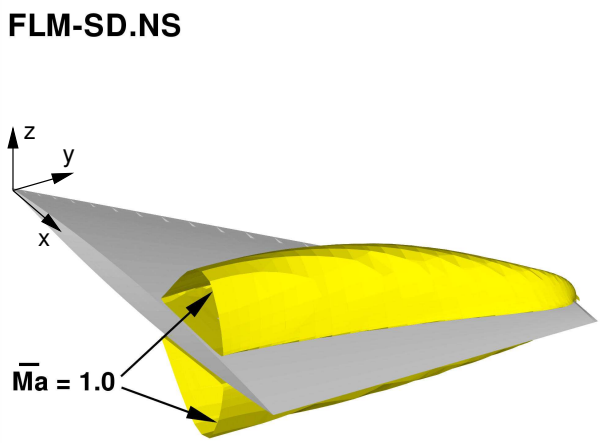

Fig. 2 Sonic isosurface of the time-invariant mean flowfield employed by FLM-SD.NS in the NCDW case 90D5

SD.NS-computed surface pressure distributions for 90D5 are composited with their FLM-NS, FLM-SDEu / FLM-Eu, and experimental counterparts in Fig. 3. The FLM-SD.NS result is described in the following: Upper- and lower-surface c_p^0, of course, exhibit symmetry, falling below $\bar{c}_{p,crit} = -0.2$ at $x/c = 0.43$ and $x/c = 0.29$, respectively, for the inner and outer span station. From root to tip the onset of supersonic flow moves significantly closer to the LE. Correspondingly, its termination is observed at $x/c = 0.77$ and $x/c = 0.72$ where c_p^0 again exceeds $\bar{c}_{p,crit}$ in the recompression towards the TE. Indicative of the shock base, its location

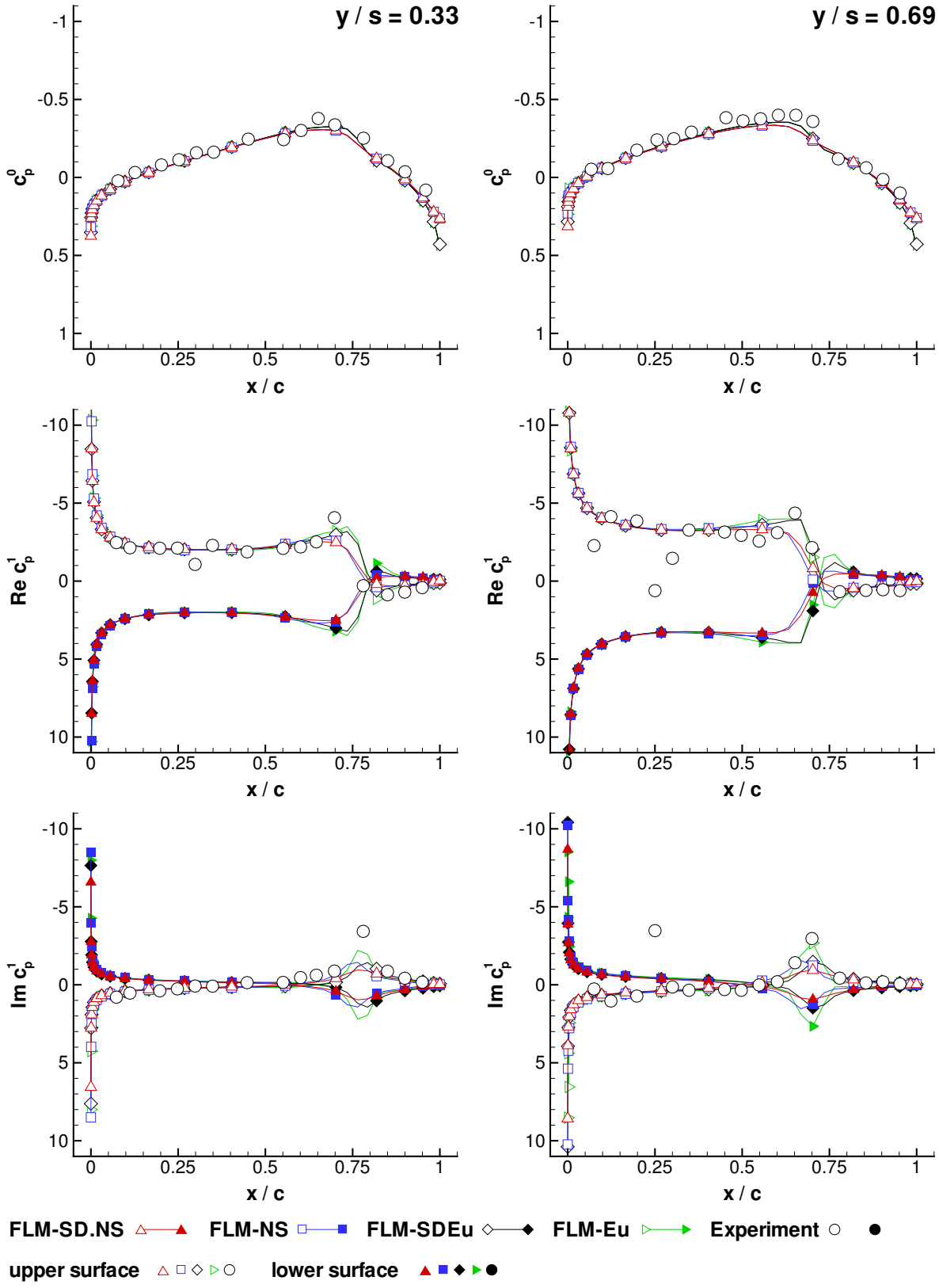

Fig. 3 Comparison of the pressure coefficient distributions for the NCDW case 90D5 ($Ma_\infty = 0.90$, $Re_\infty = 10.13 \times 10^6$, $\breve{\alpha} = 0.0$ deg, $\breve{\alpha} = 0.5$ deg, $k_{red} = 0.237$, $x_p/c_r = 0.65$)

varies far less from root to tip than that of the onset: Observed to move slightly forward relative to the local chord length, $\bar{c}_{p,crit}$ is actually reached 6% closer to the TE at the outer span station. Between the onset and termination of supersonic flow c_p^0 drops to a minimum -0.3 for both. The discontinuous recompression initiates shortly thereafter, with the weak shock merely imposing a shallow slope onto the c_p^0 progression, which decreases for the outer span station. Obviously, symmetry of the upper- and lower-surface c_p^0 yields numerically nil c_L^0 and c_M^0 values.

Complementary to c_p^0, upper- and lower-surface $Re\,c_p^1$, as well as $Im\,c_p^1$, exhibit antisymmetry: Merely considering the upper surface distribution, the sharp LE renders an initial primary peak for both $Re\,c_p^1$ and $Im\,c_p^1$, respectively, being of negative and positive value. Immediately downstream, $Re\,c_p^1$ acutely increases before leveling off at a value of -2.0 for the inner span station, and -3.0 for the outer one. In case of the former, a mild secondary $Re\,c_p^1$ peak emerges at the location of minimum c_p^0. It leads into a strong increase across the shock region, culminating in a reversal of sign for $Re\,c_p^1$ at the location of the terminating $\bar{c}_{p,crit}$. Subsequently, the $Re\,c_p^1$ progression follows through to post-shock positivity. It reaches a maximum value of $+0.3$ before decreasing towards the TE, where equalization with the lower-surface $Re\,c_p^1$ occurs at nil value. For the outer span station, the further $Re\,c_p^1$ progression towards the TE qualitatively corresponds to that of the inner one, however, lacks the mild secondary peak. A higher post-shock maximum value of $+0.5$ is noted. Evidently, $\Delta Re\,c_p^1$ forward of the zero-crossing supplies the bulk of $Re\,c_L^1$. Its positive contribution is only marginally compensated by the aft difference's negative one. Evaluation of $Re\,c_M^1$ proves to be more difficult, as leverage must also be taken into account: With the pitch (moment reference) axis intersecting the inner and outer span station, respectively, at $x/c = 0.52$ and $x/c = 0.13$, $\Delta Re\,c_p^1$ forward of the zero-crossing can contribute in equal magnitude both positively and negatively to $Re\,c_M^1$. The aft difference, on the other hand, makes an unambiguous positive contribution through its leverage.

For the inner span station, $Im\,c_p^1$ acutely decreases from its LE peak, leading into a nearly linear progression that ends slightly upstream of the shock region. Prior to ending, a reversal of sign is experienced. This places the subsequent shock- and post-shock progression into negative territory. With a minimum value of -0.9, a secondary peak is exhibited at the location of the terminating $\bar{c}_{p,crit}$, $Im\,c_p^1$ increasing from there towards the TE, where equalization with its lower-surface counterpart takes place at nil value. The $Im\,c_p^1$ progression of the outer span station qualitatively corresponds to that of the inner one. $Im\,c_p^1 > 0$ or $Im\,c_p^1 < 0$ is indicative of a time-dependent c_p that, respectively, leads or lags the excitation. Forward of the zero-crossing, $\Delta Im\,c_p^1$ contributes negatively to $Im\,c_L^1$, while its aft counterpart does so positively. Both are approximately equal in magnitude, largely compensating themselves in $Im\,c_L^1$. For the inner span station, the pitch axis intersects closely to the exhibited zero-crossing. Thus, both forward and aft $\Delta Im\,c_p^1$ can be said to render a negative $Im\,c_M^1$ contribution. As the intersection of the pitch axis moves closer to the LE for the outer span station, merely the aft $\Delta Im\,c_p^1$ can be ascertained to have an unambiguously negative contribution to $Im\,c_L^1$.

For the investigated span stations, FLM-SD.NS-computed c_p^0, $Re\,c_p^1$, and $Im\,c_p^1$ agree excellently with those obtained from FLM-NS. Mild discrepancies are observed in the shock- and post-shock region. Evidently, the small disturbance premise holds up under the dynamic nonlinearity of the weak shock. The FLM-SD.NS / FLM-NS conformity can be seen equal to that of FLM-SDEu / FLM-Eu. Viscous and inviscid c_p^0, however, differ only marginally in the shock region, with greater variation becoming noticeable for their $Re\,c_p^1$ and $Im\,c_p^1$ counterparts. Disregarding outliers, experimental surface pressure is reproduced well. Surprisingly, the data points rendering the $Re\,c_p^1$ and $Im\,c_p^1$ secondary peak are best met by the FLM-Eu computation.

Focusing on the computed global load co-

efficients (Tab. 3) $Re\,c_L^1$ gained from FLM-SD.NS agrees excellently to its FLM-NS counterpart. $Im\,c_L^1$, on the other hand, is predicted 10% higher in absolute value. This deviation,

Method	c_L^0	$Re\,c_L^1$	$Im\,c_L^1$
FLM-SD.NS	0.000	3.748	-0.013
FLM-NS	0.000	3.762	-0.012
FLM-SDEu	0.000	3.956	-0.013
FLM-Eu	0.000	3.962	0.007

Method	c_M^0	$Re\,c_M^1$	$Im\,c_M^1$
FLM-SD.NS	0.000	0.322	-0.178
FLM-NS	0.000	0.333	-0.196
FLM-SDEu	0.000	0.271	-0.196
FLM-Eu	0.000	0.285	-0.222

Table 3 Comparison of the global load coefficients for NCDW case 90D5

however, becomes acceptable when taking the two orders of magnitude into account that separate $Re\,c_L^1$ from $Im\,c_L^1$. The minute $Im\,c_L^1$ indicates a time-dependent c_L almost entirely in phase with the excitation, that is, lagging ($Im\,c_L^1 < 0$) only marginally in its evolution. Both FLM-SDEu- and FLM-Eu-computed $Re\,c_L^1$ are 5% higher than their viscous counterparts, attributable to the differing prediction of $Re\,c_p^1$ in the shock region. Their mutual deviation is similarly negligible. With FLM-SDEu $Im\,c_L^1$ is gained equal to its FLM-SD.NS-predicted instance, discounted viscosity apparently having no impact. Surprisingly, $Im\,c_L^1$ obtained from FLM-Eu exhibits a positive sign, while remaining within the same order of magnitude as its FLM-SDEu counterpart: In the shock region $\Delta Im\,c_p^1$ yields a positive $Im\,c_L^1$ contribution, which in case of FLM-Eu exceeds the negative $Im\,c_L^1$ contribution experienced from the LE to the shock-upstream zero-crossing.

FLM-SD.NS-computed $Re\,c_M^1$ and $Im\,c_M^1$ are, respectively, 3% and 9% lower in absolute value than their FLM-NS counterparts. Evidently, the deviation exhibited in $Im\,c_L^1$ has followed through to $Im\,c_M^1$. $Re\,c_M^1$ and $Im\,c_M^1$ are now in the same order of magnitude. With $Im\,c_M^1 < 0$ the time-dependent c_M clearly lags the excitation, which in case of a free pitching oscillation would have a damping effect. FLM-SDEu- and FLM-Eu-computed $Re\,c_M^1$ are, respectively, 16% and 14% lower than their viscous counterparts. The particular $Im\,c_M^1$ instances, on the other hand, are 10% and 13% higher in absolute value: Discounted viscosity has a more noticeable impact on c_M^1 than on c_L^1, with the inviscid $Im\,c_M^1$ indicating greater dynamic stability. Deviation between FLM-SDEu- and FLM-Eu-computed instances is similar to the one shown by the corresponding viscous methods.

Overall, FLM-SD.NS renders the unsteady loading of the weak shock case in very good agreement to FLM-NS. For either method, however, the viscous consideration yields only marginal improvement over the respective inviscid approach.

3.2 Medium Strength Shock / Leading Edge Vortex Case

For $Ma_\infty = 0.90$, $Re_\infty = 10.04 \times 10^6$, and $\breve{\alpha} = 3.97$ deg the FLM-NS supplied time-invariant mean flowfield exhibits an expanded supersonic region in proximity to the upper wing surface. It extends from the root to the tip, terminating with a medium strength shock significantly upstream of the TE (Fig. 4). At the root, the sharp LE additionally initiates a vortex that progresses towards the tip (Fig. 5). The LE itself approximately renders the line of separation, while the line of reattachment is observed at a sweep angle of 56 deg. Designated the LEV, it induces a localized suction plateau on the upper surface which increases in both intensity and expansion over the course of the progression, $\bar{c}_p$ reaching its minimum at the tip-proximate LE. Towards the tip the LEV eventually intersects the shock, the interaction between the two rendering a quite intricate flow topology. FLM-SD.NS-computed surface pressure distributions for 90D29 are composited with their FLM-NS, FLM-SDEu / FLM-Eu, and experimental counterparts in Fig. 6. A description of the FLM-SD.NS result is foregone.

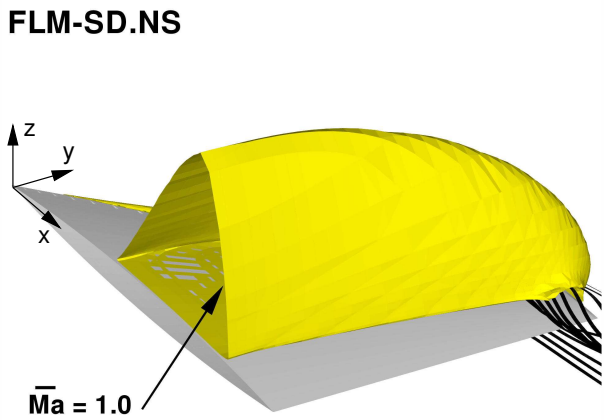

Fig. 4 Sonic isosurface of the time-invariant mean flowfield employed by FLM-SD.NS in the NCDW case 90D29

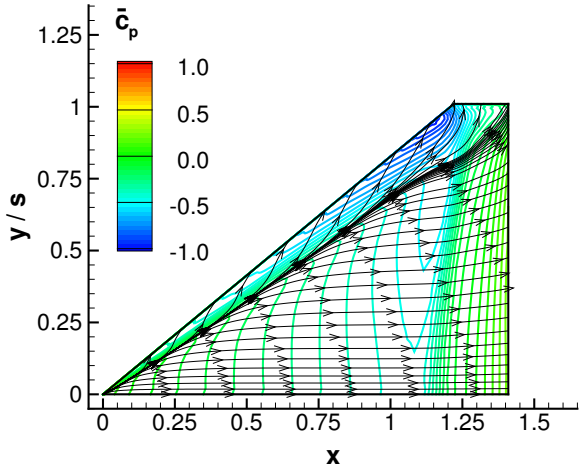

Fig. 5 Near-surface streamlines and surface isobars of the time-invariant mean flowfield employed by FLM-SD.NS in the NCDW case 90D29

For the investigated span stations, FLM-SD.NS-computed upper- and lower-surface c_p^0 agrees excellently with those obtained from FLM-NS. Respective $Re\,c_p^1$, mild discrepancies are observed for the predicted LEV- and shock-induced peaks of the inner span station, however, growing larger for the outer one. Post-shock deviations are also witnessed here for both the upper- and lower-surface $Re\,c_p^1$ progression towards the TE. Otherwise, the lower-surface $Re\,c_p^1$ agrees excellently, as linear flow physics are dominant. The same can be said for the lower-surface $Im\,c_p^1$. In regard to upper-surface $Im\,c_p^1$, mild discrepancies are observed for the predicted LEV- and shock-induced peaks of the inner span station, which yet again increase for the outer one. Here the deviation between the FLM-SD.NS and FLM-NS predicted shock-induced peak becomes very substantial, indicating that the premise of the dynamically linear approach may no longer be valid further outboard. Investigating this matter, the FLM-SD.NS-computed upper-surface c_p^0, and c_p^1 planform distributions are compared to the upper-surface c_P^0, c_p^1, c_p^2, as well as c_p^3 planform distributions gained from FLM-NS (Fig. 7 and Fig. 8). Apparently, even for a small amplitude of $\breve{\alpha} = 0.5$ deg the imposed motion on the LEV and its dynamic interaction with the shock are sufficient to induce higher-order harmonics within the time-dependent evolution of the upper-surface c_p. It can be observed, that both c_p^2 and c_p^3 locally exceed the given 10% c_p^1 range, in parts significantly. For regions where $c_p^0 \gg c_p^1 \gg c_p^2 \gg c_p^3$ no longer holds true, the small disturbance method cannot render an accurate c_p^1 prediction: As higher-order harmonics become dominant in the flowfield they exert influence on those of lower order. Consequently, the actual zeroth-harmonic flowfield will depart from the time-invariant mean one employed by the dynamically linear approach.

FLM-SD.NS / FLM-NS conformity can again be seen equal to that of FLM-SDEu / FLM-Eu, with exception of the LE region, where the former deviate less. Characteristically, the inviscid methods compute an LEV-induced upper-surface c_p^0-peak instead of the viscous observed suction plateau. This results from a separation mechanism driven by numerical instead of physical viscosity. Furthermore, the discontinuous c_p^0 compression is predicted farther downstream. Both the LEV-induced $Re\,c_p^1$- and $Im\,c_p^1$-peak are predicted closer to the LE, as well as more pro-

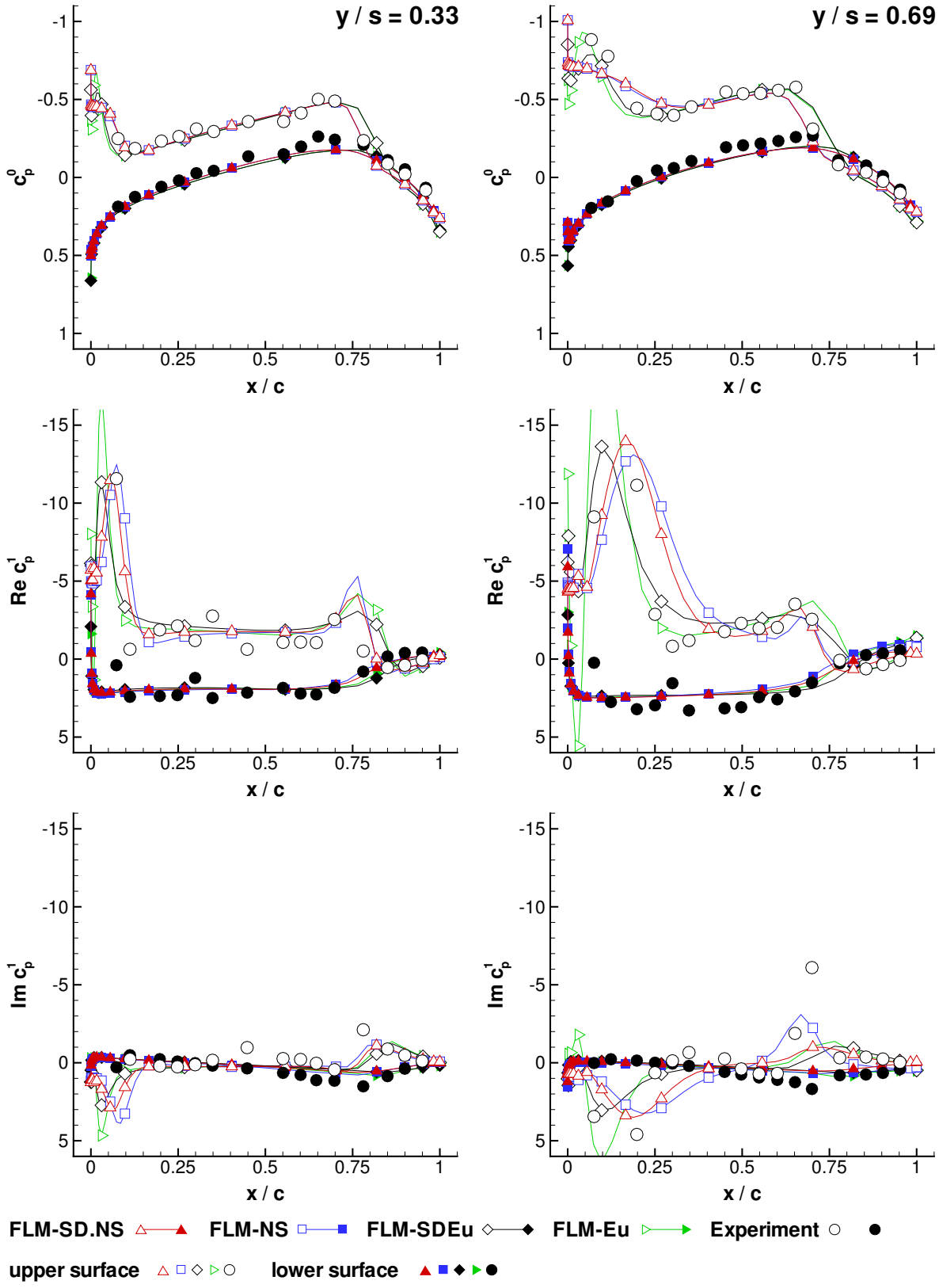

Fig. 6 Comparison of the pressure coefficient distributions for the NCDW case 90D29 ($Ma_\infty = 0.90$, $Re_\infty = 10.04 \times 10^6$, $\breve{\alpha} = 3.97$ deg, $\hat{\alpha} = 0.5$ deg, $k_{red} = 0.240$, $x_p/c_r = 0.65$)

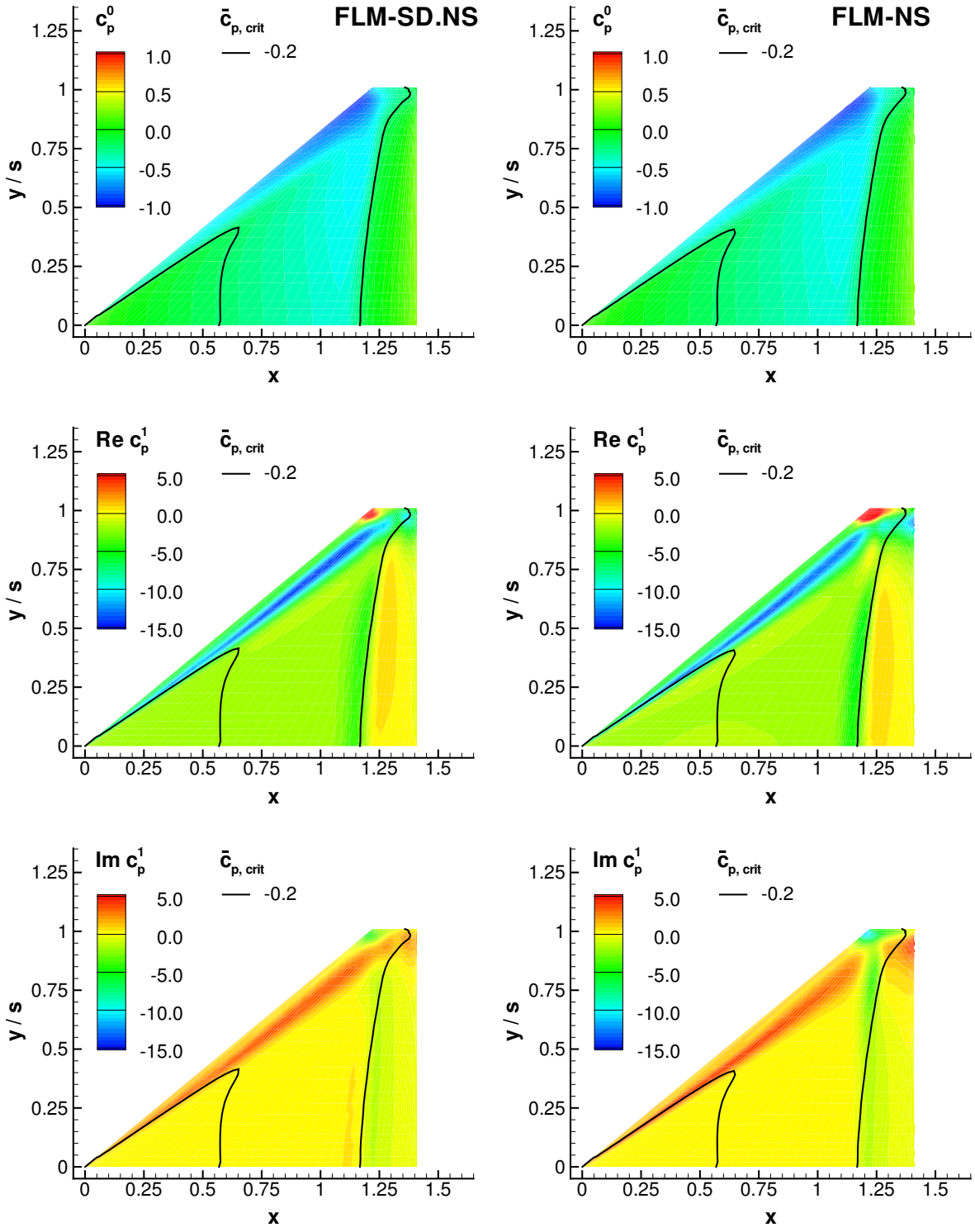

Fig. 7 Comparison of the FLM-SD.NS and FLM-NS computed planform upper-surface c_p^0, c_p^1 distributions for the NCDW case 90D29 ($Ma_\infty = 0.90$, $Re_\infty = 10.04 \times 10^6$, $\breve{\alpha} = 3.97$ deg, $\breve{\alpha} = 0.5$ deg, $k_{red} = 0.240$, $x_p/c_r = 0.65$)

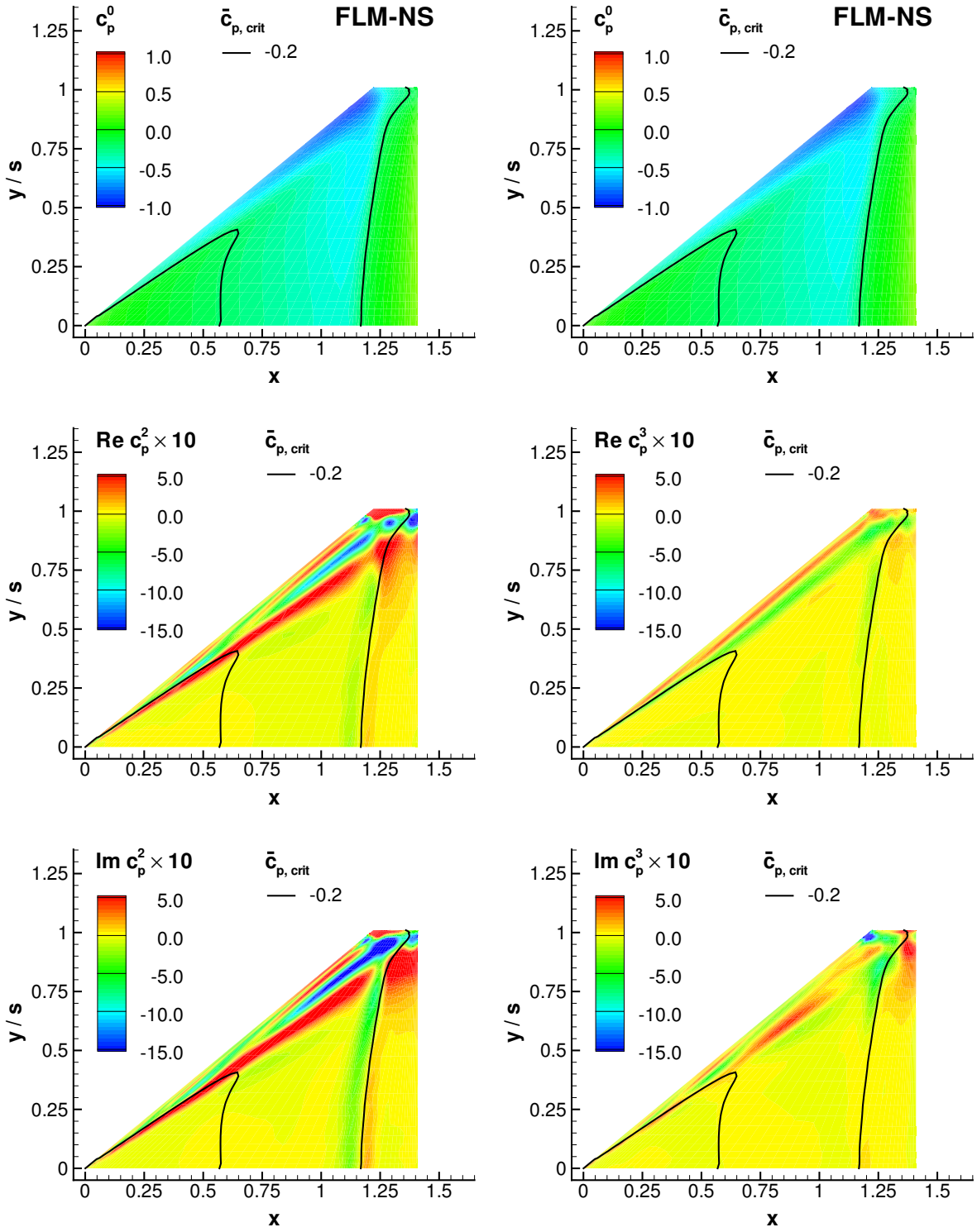

Fig. 8 Comparison of the FLM-NS computed planform upper-surface c_p^0, c_p^2, c_p^3 distributions for the NCDW case 90D29 ($Ma_\infty = 0.90$, $Re_\infty = 10.04 \times 10^6$, $\breve{\alpha} = 3.97$ deg, $\breve{\dot{\alpha}} = 0.5$ deg, $k_{red} = 0.240$, $x_p/c_r = 0.65$)

nounced. In this regard, the experimental data is better reproduced by the inviscid methods, which is surprising. Neither FLM-SD.NS / FLM-NS nor FLM-SDEu / FLM-Eu, however, are able to render the measured Imc_p^1-peak at the shock location of the outer span station.

Considering the computed global load coefficients (Tab. 4), FLM-SD.NS-predicted c_L^0 equals its FLM-NS counterpart, while Rec_L^1 is merely 3% higher. Imc_L^1, on the other hand, deviates

Method	c_L^0	Rec_L^1	Imc_L^1
FLM-SD.NS	0.263	4.065	-0.180
FLM-NS	0.263	3.958	-0.051
FLM-SDEu	0.274	4.066	-0.097
FLM-Eu	0.273	4.062	-0.064

Method	c_M^0	Rec_M^1	Imc_M^1
FLM-SD.NS	0.030	0.335	-0.178
FLM-NS	0.030	0.377	-0.229
FLM-SDEu	0.025	0.294	-0.192
FLM-Eu	0.026	0.290	-0.221

Table 4 Comparison of the global load coefficients for NCDW case 90D29

by half an order of magnitude. The minuteness of either Imc_L^1 in comparison to the correspondent Rec_L^1, however, makes this circumstance again tolerable: Both computations still indicate a time-dependent c_L that minimally lags the excitation. Whereas the artificial recomposition of the FLM-SD.NS-obtained Rec_M^1 and Imc_M^1 for the time domain would render a distinct elliptical evolution when plotted over the incidence angle, the FLM-NS counterpart would be comparably observed as collapsing to a line, however, not as distinct as for 90D5. The deviation itself can be made attributable to the differing Imc_p^1 predictions in the outboard shock region, FLM-SD.NS rendering a less positive or even negative ΔImc_p^1 contribution compared with FLM-NS. Discounting viscosity yields a 4% higher c_L^0, while having only marginal impact on Rec_L^1. The FLM-SD.Eu- and FLM-Eu-computed instances can be considered identical. Both Imc_L^1 now fall within the range set up by the FLM-SD.NS and FLM-NS computed value, their mutual deviation reducing significantly.

FLM-SD.NS-predicted c_M^0 equals its FLM-NS counterpart, while both Rec_M^1 and Imc_M^1 are gained lower in absolute value, respectively, by 11% and 22%. Comparable to 90D5, Rec_M^1 and Imc_M^1 are in the same order of magnitude. The time-dependent c_M clearly lags the excitation, again indicating a damping effect on the free pitching oscillation. The deviation between the FLM-SD.NS-computed c_M^1 and its FLM-NS counterpart are attributable to the higher-order harmonics identified in the FLM-NS-computed upper-surface c_p. Their influence follows through to the time-dependent c_M evolution from which c_M^1 is extracted. FLM-SDEu- and FLM-Eu-computed c_M^0 (Rec_M^1) are, respectively, 17% (12%) and 13% (23%) lower than their viscous counterparts. For c_M^0 the deviation experienced between the inviscid methods is equal to that of c_L^0, while the Rec_M^1 instances can be considered identical. Discounted viscosity has only limited impact on Imc_M^1, and thus on the degree of dynamic stability, both values again falling within the range of the FLM-SD.NS and FLM-NS computation. Their mutual deviation, however, reduces to 13%.

Overall, FLM-SD.NS renders the unsteady loading of the medium strength shock / LEV case in satisfactory agreement to FLM-NS. For either method the viscous consideration mainly improves on the global load coefficients' zeroth and real-part first harmonic, with the imaginary part being only marginally influenced.

3.3 Strong Shock Case

For $Ma_\infty = 0.94$, $Re_\infty = 10.06 \times 10^6$, and $\breve{\alpha} = 0.0$ deg the FLM-NS supplied time-invariant mean flowfield exhibits a sizeable, equally developed supersonic region in proximity to the upper and lower wing surface. It extends, respectively, from the root to considerably beyond the tip, terminating with a strong shock slightly upstream of the TE (Fig. 9). The discontinuous recompression is

substantial enough to induce post-shock flow separation from $y/s = 0.8$ to the tip. FLM-SD.NS-

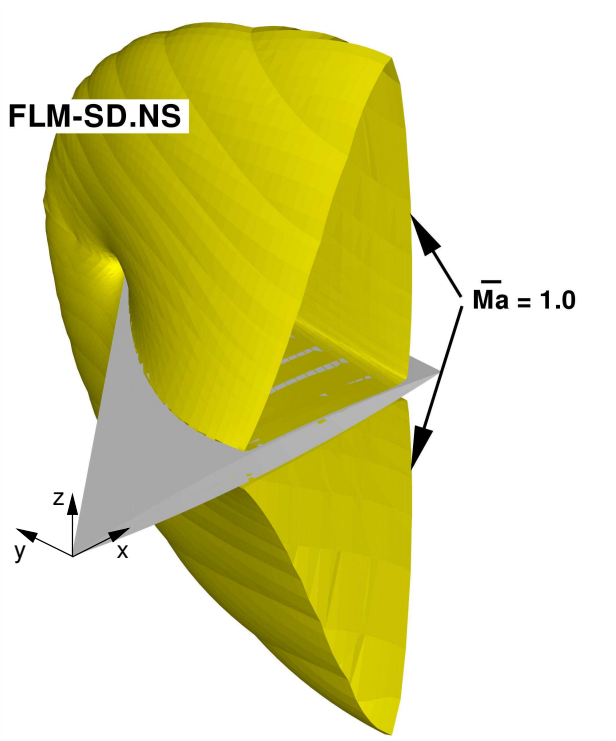

Fig. 9 Sonic isosurface of the time-invariant mean flowfield employed by FLM-SD.NS in the NCDW case 94D5

computed surface pressure distributions for 94D5 are composited with their FLM-NS, FLM-SDEu / FLM-Eu, and experimental counterparts in Fig. 10. The FLM-SD.NS result is described in the following, however, being qualitatively similar to 90D5, in not as much detail: Upper- and lower-surface c_p^0, of course, exhibit symmetry, falling below $\bar{c}_{p,crit} = -0.1$ at $x/c = 0.31$ and $x/c = 0.17$, respectively, for the inner and outer span station. The onset of supersonic flow flow occurs significantly upstream of the obtained 90D5 locations. Correspondingly, its termination moves farther downstream, c_p^0 again exceeding $\bar{c}_{p,crit}$ at $x/c = 0.89$ and $x/c = 0.87$. Between the onset and termination of supersonic flow c_p^0 drops linearly to a minimum -0.4 and -0.5, respectively, for the inner and outer span station. The discontinuous recompression initiates immediately thereafter, with the strong shock imposing a steep slope onto the c_p^0 progression, Its degree is observed to be nearly equal at both span stations. Evidently, symmetry of the upper- and lower-surface c_p^0 again yields numerically nil c_L^0 and c_M^0 values.

Complementary to c_p^0, upper- and lower-surface $Re\,c_p^1$, as well as $Im\,c_p^1$, exhibit antisymmetry: Merely considering the upper surface distribution, the sharp LE renders an initial primary peak for both $Re\,c_p^1$ and $Im\,c_p^1$, respectively, being of negative and positive value. Immediately downstream, $Re\,c_p^1$ acutely increases before merging into a positively-sloped linear progression that abruptly culminates in a shock-region reversal of sign. The initiation of the slope occurs at a lower $Re\,c_p^1$ for the outer span station than for the inner one, while being of steeper degree. For the inner span station, the zero-crossing occurs near the location of the terminating $\bar{c}_{p,crit}$, while for the outer one, at the location of minimum c_p^0. Whereas the subsequent $Re\,c_p^1$ progression conforms to the one of 90D5 for the inner span station, a secondary peak of $+4.0$ value emerges for the outer one. The associated $\Delta Re\,c_p^1$ provides for a more negative shock- / post-shock-region contribution to $Re\,c_L^1$ and thus a more positive one to $Re\,c_M^1$ than seen for 90D5. Characteristics of the 90D5 $Im\,cp^1$ progression are equally retained, however, with strongly subdued secondary peaks rendered in the shock region. For the inner span station, an additional zero-crossing is observed prior to the shock region, reversing the secondary peak's contribution to $Im\,c_L^1$ from positive to negative, and thus the contribution to $Im\,c_M^1$ vice versa.

For the investigated span stations, FLM-SD.NS-computed c_p^0, $Re\,c_p^1$, and $Im\,c_p^1$ agree excellently with those obtained from FLM-NS. This is especially true outside of the shock- and post-shock region where linear flow physics dominate. Discrepancies are merely seen with the farther upstream prediction of the $Re\,c_p^1$-zero-crossing at the inner span station, as well as the value of the $Re\,c_p^1$-secondary-peak at the outer one. For both span stations discrepancies in the $Im\,c_p^1$-secondary-peak are also noticeable. FLM-

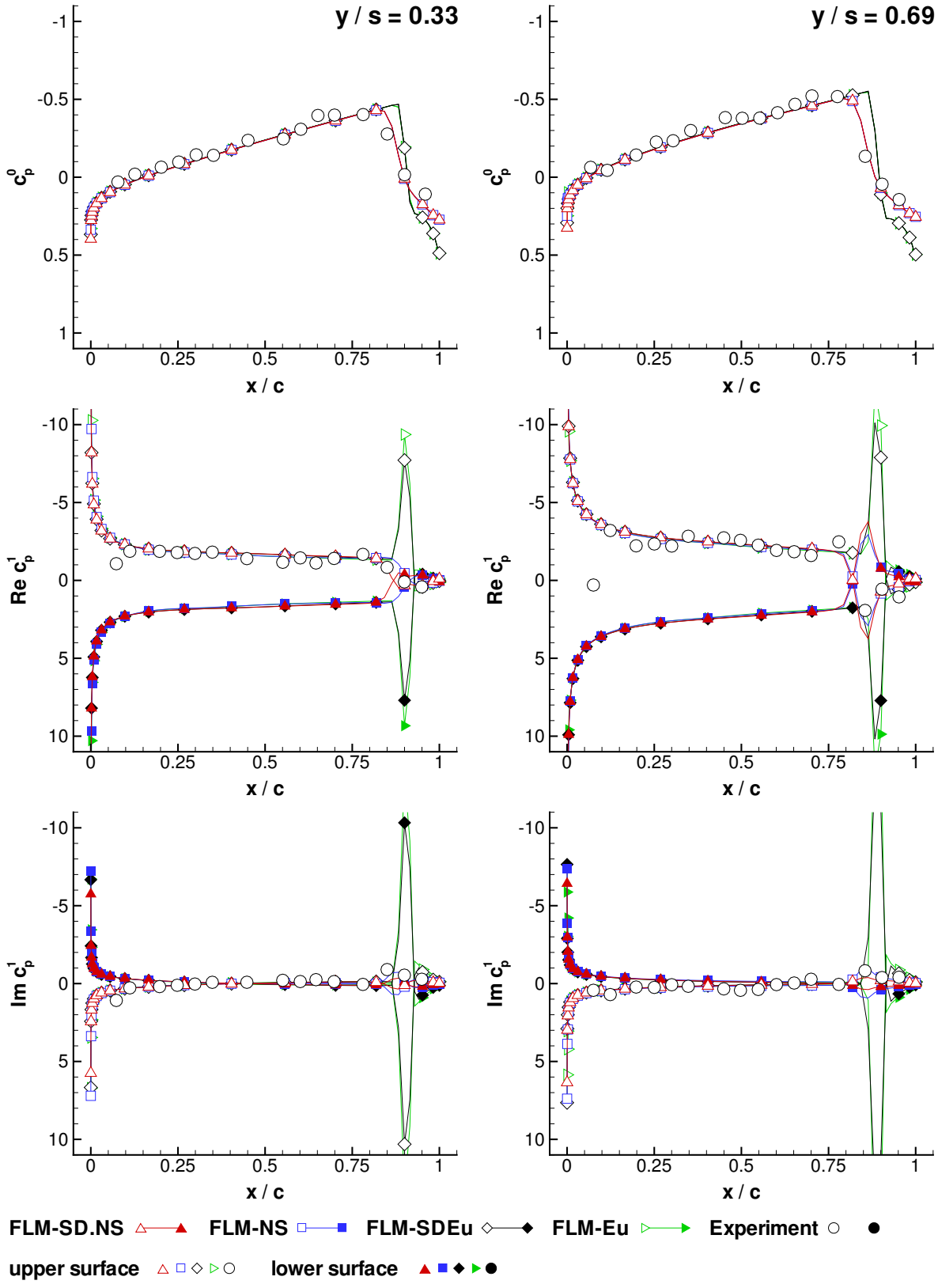

Fig. 10 Comparison of the pressure coefficient distributions for the NCDW case 94D5 ($Ma_\infty = 0.94$, $Re_\infty = 10.06 \times 10^6$, $\breve{\alpha} = 0.0$ deg, $\breve{\alpha} = 0.5$ deg, $k_{red} = 0.230$, $x_p/c_r = 0.65$)

SD.NS / FLM-NS conformity can again be seen equal to that of FLM-SDEu / FLM-Eu. The inviscid methods compute a profoundly differing behavior in the shock- and post-shock region. Not only is the discontinuous c_p^0 recompression predicted farther downstream, strong $Re\,c_p^1$- and $Im\,c_p^1$-peaks are rendered at its location, respectively, making substantial $Re\,c_L^1$, $Re\,c_M^1$ and $Im\,c_L^1$, $Im\,c_M^1$ contributions. Experimental surface pressure is best reproduced by FLM-SD.NS / FLM-NS, confirming the higher fidelity of the viscous approach.

Regarding the computed global load coefficients (Tab. 5), $Re\,c_L^1$ obtained from FLM-SD.NS can be considered identical to its FLM-NS counterpart. $Im\,c_L^1$, on the other hand, is predicted 17% lower in absolute value, attributable to differingly computed $Im\,c_p^1$ in the shock region. Similar to 90D29, an order of magnitude separates $Re\,c_L^1$ and $Im\,c_L^1$. The latter's minuteness indicates a time-dependent c_L that lags the excitation by only a small margin, yet in comparison to 90D5 again exhibits a distinct elliptical evolution when plotted over the incidence angle. Both FLM-SDEu- and FLM-Eu-computed $Re\,c_L^1$ are significantly higher than their viscous counterparts: The strong $Re\,c_p^1$-peaks rendered in the shock region yield a large yet chordwise-localized difference between upper- and lower-surface distribution. Contributing positively, its summation over the semi-span, however, is substantial enough to increase $Re\,c_L^1$ by 23% on average. This circumstance emerges even more pronounced in $Im\,c_L^1$: Outside of the shock region $\Delta Im\,c_p^1$ would merely result in a minutely negative $Im\,c_L^1$ similar to that of the viscous computations. Comparatively, the $Re\,c_p^1$-corresponding $Im\,c_p^1$-peaks contribute strongly negative to $Im\,c_L^1$. Supplying the bulk of its value, a fourfold amplification of the viscously obtained $Im\,c_L^1$ is experienced. The deviation between FLM-SDEu- and FLM-Eu-computed $Re\,c_L^1$, as well as $Im\,c_L^1$, becomes similar to that of the respective FLM-SD.NS and FLM-NS counterparts.

Method	c_L^0	$Re\,c_L^1$	$Im\,c_L^1$
FLM-SD.NS	0.000	3.301	-0.181
FLM-NS	0.000	3.302	-0.218
FLM-SDEu	0.000	4.087	-0.808
FLM-Eu	0.000	4.034	-0.947

Method	c_M^0	$Re\,c_M^1$	$Im\,c_M^1$
FLM-SD.NS	0.000	0.311	-0.077
FLM-NS	0.000	0.284	-0.072
FLM-SDEu	0.000	-0.016	0.197
FLM-Eu	0.000	-0.019	0.254

Table 5 Comparison of the global load coefficients for NCDW case 94D5

FLM-SD.NS predicts both $Re\,c_M^1$ and $Im\,c_M^1$ within 10% of the FLM-NS-gained value, the two being separated by merely half an order of magnitude. Even though $Re\,c_L^1$ has been established as identical between the two methods, the same cannot be said for $Re\,c_M^1$. Inversely, the deviation exhibited by $Im\,c_L^1$ does not entirely follow through to $Im\,c_M^1$. Considering skin friction's contribution to be negligible, deviations in $Re\,c_p^1$ are apparently amplified towards $Re\,c_M^1$, while deviations in $Im\,c_p^1$ are compensated towards $Im\,c_M^1$, for the given reference axis. However, the fundamental difference in the small disturbance and the dynamically fully nonlinear method's manner of assessing the global load coefficients must again again be taken into account: Regarding the FLM-NS-computed c_M evolution over the incidence angle, an antisymmetric influence becomes evident in proximity of both the upper and lower dead center. It results from the expansion and contraction of the separated flow region over the course of a cycle. Even though the first harmonic still dominates the c_M evolution, the contained higher-order harmonics are again no longer as negligible as postulated by the small disturbance premise, thus allowing for the c_M^1 deviation. The time-dependent c_M is predicted to lag the excitation, yet not as strongly as it did in 90D5 and 90D29.

Discounting viscosity, the character of c_M becomes significantly altered: FLM-SDEu- / FLM-

Eu-computed $Re\,c_M^1$ and $Im\,c_M^1$ exchange sign as well as order of magnitude given by their viscous counterparts. Through accounted leverage, the inviscidly predicted $Re\,c_p^1$- and $Im\,c_p^1$-peaks in the shock region, respectively, supply the bulk negative and positive contribution that tip the scale. With $Im\,c_M^1 > 0$ the time-dependent c_M now leads the excitation, even doing so by slightly more than a quarter cycle. In case of a free pitching oscillation this would have an amplifying effect. For both $Re\,c_M^1$ and $Im\,c_M^1$ deviation between the FLM-SDEu and FLM-Eu-computed instance is within 20% – double the one exhibited between the viscous counterparts. Whereas this appears reasonable for $Re\,c_M^1$ on grounds of its minuteness, it seems surprisingly high for $Im\,c_M^1$. Evidently, the deviation compensates itself in the phase shift of the time-dependent c_M yet persists in its magnitude.

Overall, FLM-SD.NS renders the unsteady loading of the strong shock case in good agreement to FLM-NS. For either method, the viscous consideration yields a substantial improvement over the respective inviscid approach: The more complete flow model contrarily indicating dynamic stability.

4 Computational Efficiency

FLM-SD.NS and FLM-NS computation times, as well as the inverse ratio between the two are summarized in Table 6. Evidently, FLM-SD.NS realizes reductions up to an order of magnitude: Whereas $\check{t}_{CPU}^{SD.NS}$ are all around 24 h, a far greater range can be observed for $\check{t}_{CPU}^{NS}$, the computation of 90D5 and 94D5 taking longer than 90D29 by multiples. At default settings, the fully dynamical nonlinear treatment of the $\breve{\alpha} = 0$ deg incidence motion had exhibited solution instabilities towards the upper / lower dead center, that is, at physical time-steps where the deflected wing experiences strong de- and acceleration. Merely very high instances of implicit damping allowed for a remedy, significantly drawing out the computation in turn. The decreased ζ_{CPU} witnessed for 94D5 stems in part from the employed higher-clocking processor, accelerating FLM-NS considerably more than FLM-SD.NS. With 1.7 GByte RAM, FLM-SD.NS allocates four times more working memory than FLM-NS, as both complex amplitude and time-invariant mean entities need to be stored. It is the tradeoff made towards superior computational efficiency.

Case	$\check{t}_{CPU}^{SD.NS}$, h	$\check{t}_{CPU}^{NS}$, h	ζ_{CPU}
90D5	24.1	419.8	17.4
90D29	21.2	71.3	3.4
94D5	17.2	242.7	14.1

Table 6 Comparison of computational effort between FLM-SD.NS and FLM-NS for the NCDW cases

5 Conclusions

In an effort to further substantiate FLM-SD.NS application readiness, computational results for NCDW harmonic pitching oscillations were presented and compared to those of FLM-NS, FLM-SDEu / FLM-Eu, as well as experimental data: Both a weak and a strong shock case demonstrated the small disturbance Navier-Stokes approach's accuracy and efficiency in predicting the unsteady local and global loading. Special attention had been given to the obtained Imc_m^1, as it is indicative of the corresponding free oscillation's amplified or damped state. In this regard, the strong shock case illustrates the benefit of the viscous consideration, FLM-SD.NS / FLM-NS predicting dynamic stability where FLM-SD.Eu / FLM-Eu does not. The medium strength shock / LEV case, on the other hand, discloses the limitations of the small disturbance approach: Fourier-analysis of the FLM-NS-computed upper-surface c_p reveals localized higher-order harmonics that are no longer negligible. They result from the LEV itself, as well as the LEV's interaction with the shock. Exerting influence on the time-dependent c_M evolution, the extracted Imc_M^1 and the FLM-SD.NS-computed one exhibit the most pronounced deviation.

To date, more application-oriented investiga-

tions have been realized with FTDW harmonic pitching oscillations: In analogy to the NCDW, a shockless case, an LEV case, and a medium strength shock case were computed. The promising results will be presented in the near future. Complementary studies for high aspect ratio wings, as well as a rectangular wing / nacelle configuration undergoing harmonic motions are on the verge of completion, while an assessment of FLM-SD.NS / FLM-SDEu prediction quality with regard to the AGARD 445.6 wing's flutter boundary has just commenced.

References

[1] Allen, A., Iatrou, M., Pechloff, A., and Laschka, B. Computation of delta wing flap oscillations with a Reynolds-averaged Navier-Stokes solver. In H.-J. Rath, C. Holze, H.-J. Heinemann, R. Henke and H. Hönlinger, editor, *New Results in Numerical and Experimental Fluid Mechanics V: Contributions to the 14th STAB-DGLR-Symposium, Bremen, Germany 2004*, pp 85–93, Berlin, Germany, 2006. Notes on Numerical Fluid Mechanics and Multidisciplinary Design, Vol. 92, Springer-Verlag.

[2] Bennett, R. M. and Walker, C. E. Computational test cases for a clipped delta wing with pitching and trailing edge control surface oscillations. NASA TM-1999-209104, 1999.

[3] Blazek, J. A multigrid LU-SSOR scheme for the solution of hypersonic flow problems. AIAA Paper 94-0062, Jan. 1994.

[4] Chakravarthy, S. R. High resolution upwind formulations for the Navier-Stokes equations. Lecture Series on Computational Fluid Dynamics, VKI 1988-05, von Karman Institute, Brussels, Belgium, March 1988, pp 1–105.

[5] Iatrou, M., Allen, A., Pechloff, A., Breitsamter, C., and Laschka, B. Small disturbance Euler/Navier-Stokes computations for delta wing flap oscillations. Advanced Vehicle Technology Meeting, NATO Research and Technology Organization, RTO-MP-AVT Paper 123-16, Budapest, Hungary, April 2005.

[6] Kreiselmaier, E., and Laschka, B. Small disturbance Euler equations: Efficient and accurate tool for unsteady load predictions. *Journal of Aircraft*, Vol. 37, No 5, pp 770–778, 2000.

[7] Markmiller, J. Validierung eines zeitechten und eines small disturbance Navier-Stokes Verfahrens an einem schwingenden Deltaflügel. Diploma Thesis TUM-FLM-2003/28, Aerodynamics Division, Institute for Fluid Mechanics, Technische Universität München, Garching, Germany, Oct. 2003.

[8] Pechloff, A. and Laschka, B. Small disturbance Navier-Stokes method: Efficient tool for predicting unsteady air loads. *Journal of Aircraft*, Vol. 43, No 1, pp 17–29, 2006.

[9] Roe, P. L. Approximate Riemann solvers, parameter vectors and difference schemes. *Journal of Computational Physics*, Vol. 43, No 2, pp 357–372, 1981.

[10] Schuster, D. M., Liu, D. D., and Huttsell, L. J. Computational aeroelasticity: Success, progress, challenge. *Journal of Aircraft*, Vol. 40, No 5, pp 843–856, 2003.

[11] Weishäupl, C., and Laschka, B. Small disturbance Euler simulations for unsteady flows of a delta wing due to harmonic oscillations. *Journal of Aircraft*, Vol. 41, No 4, pp 782–789, 2004.